JOURNAL OF PROPULSION AND POWER
Vol. 17, No. 4, July–August 2001

Actuator Duct Model of Turbomachinery Components for Powered-Nacelle Navier–Stokes Calculations

Entsung Hsiao,* Mahmood Naimi,* and Jeffrey P. Lewis†
The Boeing Company, Seattle, Washington 98124
and
Keith Dalbey,‡ Yifang Gong,§ and Choon Tan¶
Massachusetts Institute of Technology, Cambridge, Massachusetts 02139

An actuator-duct model was installed into the WIND Navier–Stokes code. With this model, the flow through fan rotors and fan exit guide vanes can be simulated without specifying a blade geometry. Flow turning, total pressure, and total temperature changes across blade rows are controlled by body forces added to the Navier–Stokes equations. This model provides an affordable and relatively accurate prediction of a three-dimensional flowfield through rotor and stator blade rows. A NASA stage 35 compressor and a NASA 22″ test rig flow were analyzed to quantify the ability of the actuator-duct theory to represent blade rows. Favorable comparisons between predicted and measured total pressure, total temperature, and swirl demonstrated that the actuator-duct model is a promising approach for predicting rotating machinery flowfields. The effect of the rotor on inlet flow separation was determined by comparing the predictions of a flow-through nacelle with the predictions using the actuator duct to simulate the rotating fan. The comparison shows that the presence of the rotor increased separation-free angle of attack over the flow-through nacelle that is consistent with experimental observations.

Nomenclature

F	=	body force
FNPR	=	fan nozzle pressure ratio
h	=	blade-to-blade gap staggered spacing
K	=	body force coefficient
P	=	pressure
rpm	=	revolutions per minute
T	=	temperature
V	=	velocity
α	=	blade metal angle
ρ	=	density

Subscripts

inf	=	free stream, reference stage
rel	=	relative stage
n	=	normal to flow direction
p	=	parallel to flow direction
r	=	radial coordinate
t	=	total stage
x	=	axial coordinate
θ	=	pitchwise coordinate

Introduction

COMPUTATIONAL fluid dynamics (CFD) has revolutionized the aerodynamic design process of propulsion system components of commercial airplanes over the last two decades. Despite the continual improvements in numerical simulations, considerable computational resources are still required to model the fan rotor and guide vane stator as part of a complete powered-nacelle simulation. It is important to include the effect of the fan rotor and stator on the inlet and nozzle design.

For subsonic inlet design, an inlet flow separation at high angle of attack or yaw operating conditions is one of the critical design considerations. The conventional method to determine if inlet flow is separated and to generate inlet distortion starts with a flow-through nacelle model that does not include the effect of a fan rotor. The effects induced by the rotor on the inlet flow include blockage, swirl, and suction. A test was conducted by NASA and Pratt and Whitney[1] to evaluate the impact of the fan on inlet separation with an advanced ducted prop 17″ rig configuration. A comparison between the results of flow-through and powered nacelles from that experiment indicates that the presence of the fan increased separation angle of attack by 3–4 deg over the flow-through nacelle. The inlet design based on the flow-through model to keep the flow attached at operating conditions with high angle of attack or yaw might be too conservative.

To determine inlet distortion and operating margin correctly, it is important to include the rotor effect in the inlet design and flow analysis process. Recently, some experimental and CFD studies were conducted using screens and rods located at the fan face to simulate the effect of a rotor in the flow-through model.[1,2] An actuator disk with a Navier–Stokes code was also used to simulate the flow through the fan rotor.[3] The actuator disk model is two-dimensional, does not include the effect of swirl, and usually requires the total pressure and total temperature change across the fan as input to the model. Another approach is the direct CFD simulation with the actual blade geometry, using the Navier–Stokes equations.[4,5] This approach requires enormous computing resources, which makes this approach impractical based on the present computing resources. With an actuator duct, the effect of blockage, swirl, and suction due to the fan rotor can be included with reasonable computing costs. The flow turning, total pressure, and total temperature change through the rotor and stator blade rows can be simulated without the actual blade geometry. This approach can provide a reasonably accurate but efficient fan rotor model for inlet flow calculations with inlet distortion at high angle-of-attack or crosswind operating conditions. In addition, this model can provide a more realistic flow condition, which includes swirl effects, for the nozzle and nacelle pylon design. With the actuator-duct model, the three-dimensional flowfield of a complete high-bypass duct system that includes the inlet, fan bypass duct, fan nozzle, and primary nozzle can be affordably and accurately predicted.

Received 12 July 2000; presented as Paper 00-4328 at the AIAA 18th Applied Aerodynamics Conference, Denver, CO, 14–17 August 2000; revision received 8 February 2001; accepted for publication 8 February 2001.

*Engineer/Scientist, Enabling Technology Research.
†Manager, Propulsion System Division.
‡Graduate Student.
§Postdoctoral Researcher, Gas Turbine Laboratory.
¶Principal Research Engineer, Gas Turbine Laboratory.

The objective of this study is to quantify the accuracy of the actuator-duct logic[6] developed by the Massachusetts Institute of Technology for predicting the flow through a high-bypass propulsion system. The problem being examined is the level of system modeling needed to enable an adequate prediction of inlet separation angle of attack with the presence of fan. A key part of this study is the installation of the actuator-duct theory into the WIND Navier–Stokes code.[7] Assessment and validation of this actuator-duct logic were performed using the experimental data from the NASA 22″ rig configuration.[8]

Actuator-Duct Logic

In the conventional actuator disk model, a plane/disk of discontinuity is used to represent a blade row. The aerodynamic flow property changes across the blade row are assumed to be concentrated at the disk. In this actuator-duct logic, the flow property changes are spread over regions of cells that span a blade region. The aerodynamic effects of a blade row are modeled through 1) the assumption of infinite blades and the axisymmetric flow in each infinitesimal blade passage and 2) body force added as the source terms of the Navier–Stokes equations. In this model, the blade force on a cascade section is separated into forces that are parallel and normal to the section mean-line. In the cylindrical coordinate system, the body force components of the blade normal and parallel forces in the axial, tangential and radial directions are expressed in the following form:

$$
\begin{aligned}
F_{n,x} &= \frac{K_n}{h}\frac{V_\theta}{V_{\text{rel}}}(V_x\cos\alpha + V_\theta\sin\alpha)\\
&\quad\times(V_\theta\cos\alpha - V_x\sin\alpha) + \frac{1}{\rho}\frac{\mathrm{d}P}{\mathrm{d}x}\sin^2\alpha\\
F_{n,\theta} &= -\frac{K_n}{h}\frac{V_x}{V_{\text{rel}}}(V_x\cos\alpha + V_\theta\sin\alpha)\\
&\quad\times(V_\theta\cos\alpha - V_x\sin\alpha) - \frac{1}{\rho}\frac{\mathrm{d}P}{\mathrm{d}x}\sin\alpha\cos\alpha\\
F_{p,x} &= -\frac{K_p}{h}V_{\text{rel}}V_x, \qquad F_{p,\theta} = -\frac{K_p}{h}V_{\text{rel}}V_\theta\\
F_{p,r} &= -\frac{K_p}{h}V_{\text{rel}}V_r
\end{aligned}
\tag{1}
$$

In the above expressions, K_n and K_p are the body force coefficients in the directions normal and parallel to the blade mean-line. V_{rel} is the blade relative velocity. V_x, V_θ, and V_r are the velocity components in the axial, tangential, and radial directions. The letters α and h are the blade metal angle and the blade-to-blade gap staggered, spacing, respectively. Further details of the body force formulation can be found in Ref. 6.

Before determining the body forces, body force coefficients at every grid point within the blade zone are needed. Body force coefficients, which represent blade characteristics, are calculated from a known flowfield around the blade. The flowfield can be generated either from test data or a direct CFD solution based on actual blade geometry. With a known flowfield around the blade, body forces are obtained by integrating forces over the computational cell, then body force coefficients are calculated from Eq. (1).

Actuator-Duct Installation

In this study, the actuator-duct logic was installed into the WIND code. WIND[7] is a Navier–Stokes code supported by the National Project for Application Oriented Research in CFD (NPARC) Alliance, which consists mainly of the NASA Glenn Research Center, the Air Force Arnold Engineering Development Center, and Boeing. The body forces are implemented as source terms in the right-hand side of the governing equations. The source terms derived from the body forces are active only within the blade zone. In general, adding the source terms explicitly to the right-hand side of the equations would cause instability in the WIND code. To stabilize the solution, source relaxation factors were introduced in the transient stage.

A NASA stage 35 compressor configuration[9] was used to verify the installation of the actuator duct. This compressor was used because its geometry is relatively simple and the data are available for the comparisons. The body force coefficients for the rotor and stator were based on measurements at the midspan and tip locations. Within the rotor and stator blade zones, body force coefficients at every grid point were set to the same values (i.e., $K_n = 4.20$ and $K_p = 0.04$). An Euler calculation was performed with WIND using the actuator duct at the 100%-speed operating condition. Figure 1 shows the computational mesh of the stage 35 compressor. The predicted swirl angle, total pressure, and total temperature profiles were compared with test data at the rotor and stator trailing edges in Fig. 2. All the qualitative flow features were predicted by the actuator duct with swirl introduced by the rotor and reduced by the stator. The predicted total pressure matched the measurements in midspan and tip locations at both the rotor and stator trailing edges. The

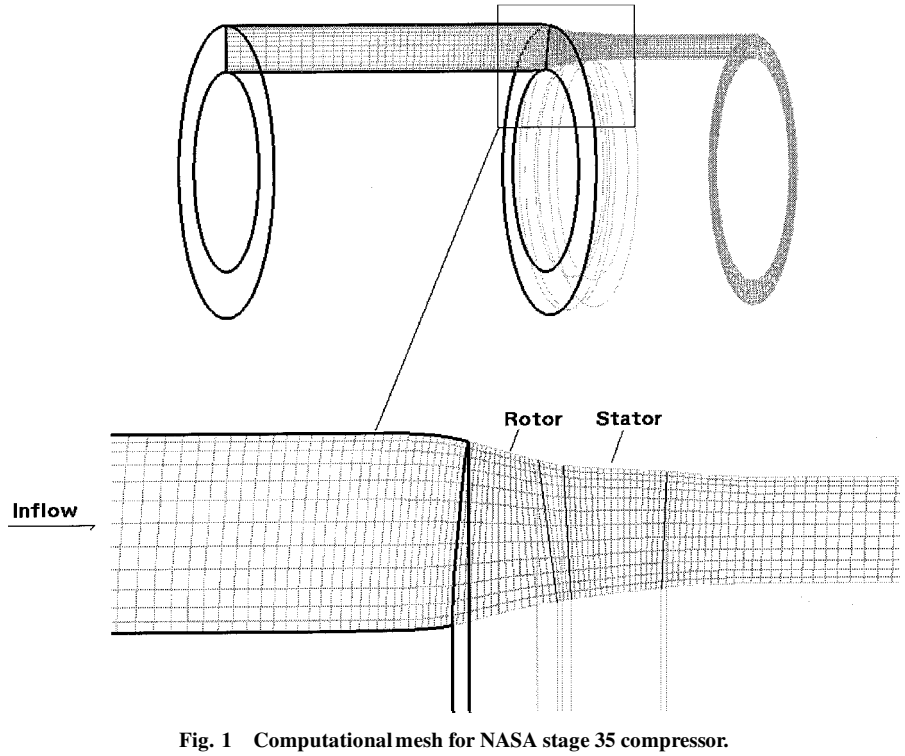

Fig. 1 Computational mesh for NASA stage 35 compressor.

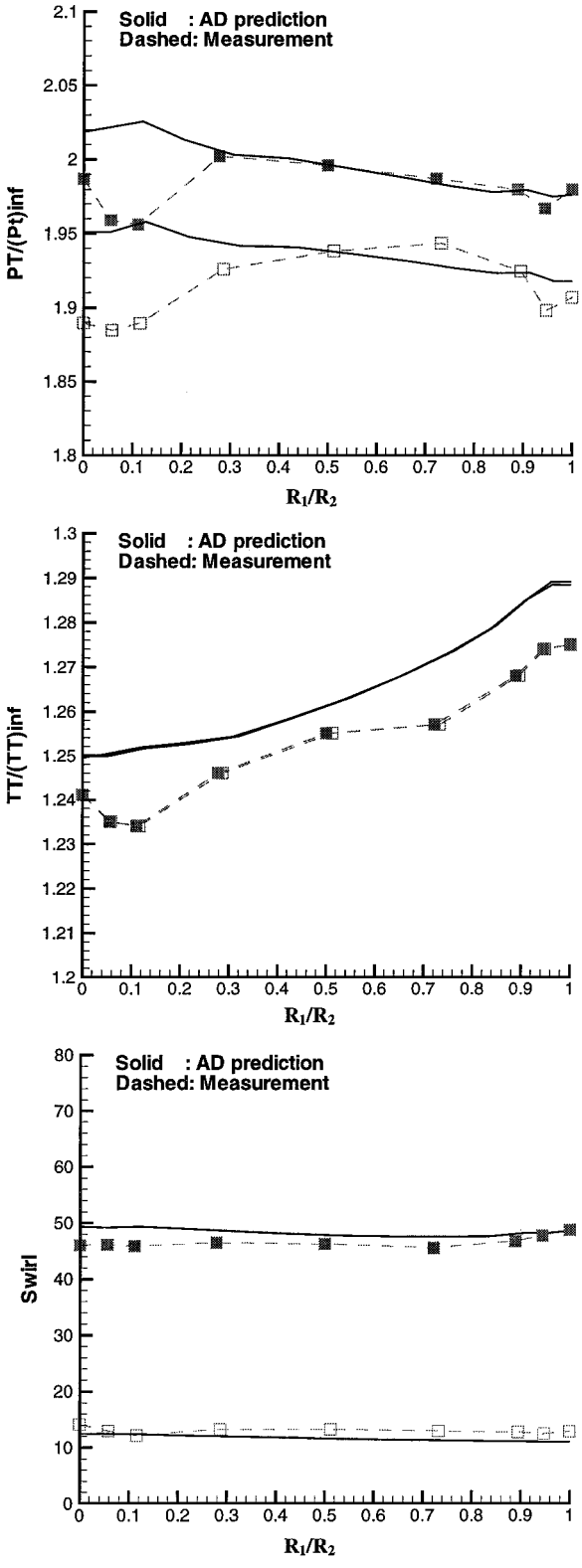

Fig. 2 Comparisons of *Pt*, *Tt*, and swirl angle profiles between actuator-duct predictions and data at rotor and stator trailing edges. $R_1 = r - r_{\text{hub}}$ and $R_2 = r_{\text{casing}} - r_{\text{hub}}$.

deviations of total pressure near the hub end-wall surface may be due to basing the body force coefficients on the midspan and tip location measurements. The actuator-duct calculation overpredicted the total temperature at the rotor and stator trailing edges, but the overall trends of the total temperature and swirl agreed well with the measurements.

It is believed that the prediction of the stage 35 compressor could be improved with a more sophisticated body force coefficient profile, such as a nonuniform coefficient profile in the radial direction. In the current study, there was no attempt to improve body force coefficients for the stage 35 compressor to better match the data, because this calculation was a check of the correct actuator-duct installation into the WIND code. This case showed that the installation was correct. The calculations of the NASA 22″ rig periodic fan exit guide Vane (FEGV) and the three-dimensional 22″ rig, to be reported in the next section, will be used to demonstrate the accuracy of the technique.

Actuator-Duct Logic Assessment

The assessment of the actuator-duct logic consisted of two parts. In the first part, a Navier–Stokes analysis of the NASA 22″ rig FEGV geometry as shown in Fig. 3 was performed for a single periodic passage with the blade geometry. Next, the result of the calculation was used to compute body force coefficients for the actuator-duct model, which was then used to perform a set of Navier–Stokes analyses without blade geometry. The assessment of the actuator-duct logic was carried out by comparing the predictions of the actuator duct with the predictions of the CFD calculation with the actual guide vane blade geometry. In the second part, a Navier–Stokes calculation using the actuator-duct logic was performed for the three-dimensional NASA 22″ rig configuration consisting of an inlet, fan duct, and fan nozzle. Flow turning, total pressure, and total temperature changes across the rotor and guide vane blade rows were simulated using the actuator duct. The predictions were compared with experimental measurements.

There are a few elements common to all of the calculations discussed in the following sections. First, the Integrated CAD Engineering and Manufacturing (ICEM) code was used to generate all of the multiblock grids used. Next, the computational analysis was performed using the WIND Navier–Stokes code with the Spalart–Allmaras one-equation turbulence model. During the calculations, the L2 norm of the residual and the mass flow rate in the fan duct were monitored. The solution was deemed converged when the mass flow rate did not change with respect to the iteration number.

NASA 22″ Rig Periodic FEGV Calculation with Guide Vane Geometry

Before the calculations using the actuator duct were attempted, a direct CFD calculation was carried out for a single blade passage of the actual FEGV geometry. These single-blade passage calculations will be used later to generate the body force terms for the actuator-duct calculations, and to compare with the actuator-duct predictions of total pressure, total temperature, and swirl angles.

Two guide vane configurations were used in this calculation: a fan-1 configuration, with 45 vanes, and a fan-2 configuration, with 51 vanes. The computational domain contains one guide vane passage with a periodic boundary condition at the circumferential boundary. The computational meshes were generated with the fine grid packed around the nozzle and guide vane surfaces to resolve the viscous boundary layer. Approximately 3.5 million grid points were used. For each configuration, calculations were made at three

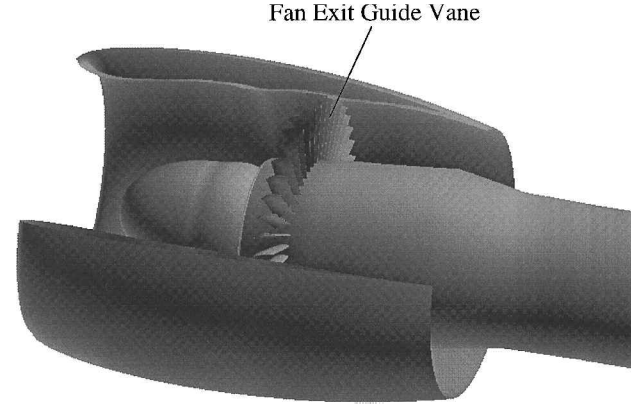

Fig. 3 NASA 22″ rig fan-1 configuration.

Table 1 Configurations and operating conditions for NASA 22″ rig periodic FEGV calculation

Configuration	Number of guide vanes	Operating Condition rpm	FNPR
Fan-1	45	7710	1.23
		8740[a]	1.30[a]
		9900	1.33
Fan-2	51	6950	1.23
		7870[a]	1.30[a]
		8300	1.33

[a]Design operating condition.

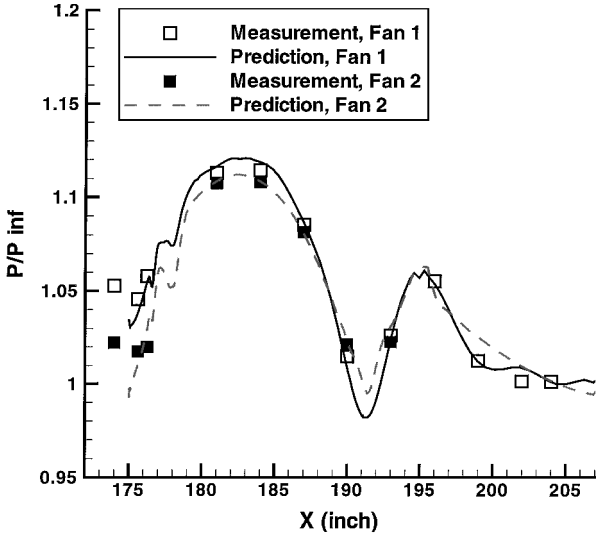

Fig. 4 Comparison of wall static pressure along fan duct inner wall for fan-1 at 8740 rpm and fan-2 at 7870 rpm.

different operating conditions, as summarized in Table 1. The inflow total pressure, total temperature, and swirl angle profiles were specified at the nozzle inflow plane (i.e., station 12.5).

The predictions using the blade geometry were compared with the test data (fan nozzle wall static pressure) before they were used to derive the guide vane body force coefficients. Figure 4 shows that the predicted static pressure distributions along the fan duct correspond favorably with the measurements. This demonstrates that the CFD prediction with the actual guide vane geometry has the required fidelity for assessing the actuator-duct accuracy.

NASA 22″ Rig Periodic FEGV Actuator-Duct Calculation

The NASA 22″ rig periodic FEGV configuration calculations using an actuator duct are presented in two sections. In the first section, generation of the body force coefficients used to represent FEGV blade characteristics is described. The second section presents an assessment of the actuator-duct logic in simulating flow turning and loss through the FEGV. The predicted flowfields for the calculations that used the actuator duct were compared with those from the direct CFD calculation with the guide vane geometry.

Generation of Body Force Coefficients

In this FEGV calculation, the guide vane body force coefficients were generated using the CFD predicted flowfield as presented in the preceding section. Ideally, the actuator-duct prediction should match the result of the blade-geometry–based CFD calculation if the guide vane characteristics were represented correctly by the body force coefficients.

The procedure for generating body force coefficients from a CFD solution is a reverse process of determining body forces from Eq. (1). Using this procedure, body forces at each computational grid point within the blade zone are calculated from a given three-dimensional flowfield. An axisymmetric flowfield is first generated from a three-dimensional flowfield by averaging the flow parameters in the circumferential direction. The body forces are extracted from this circumferentially averaged flow and are therefore also axisymmetric.

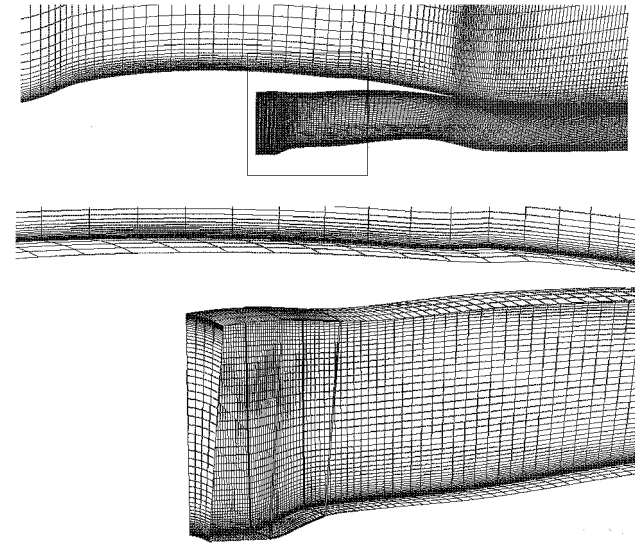

Fig. 5 Computational mesh for NASA 22″ rig periodic FEGV calculation using actuator duct.

With those flow parameters and body forces, the body force coefficients at each computational point within the blade zone can be obtained from Eq. (1) because the blade geometry is known. The resultant body force coefficients are uniform circumferentially. In these calculations, the FEGV body force coefficients for the fan-1 and fan-2 configurations were generated using the CFD solutions at design operating conditions, and those coefficients were applied to the calculations at other operating conditions.

Computation with Actuator Duct

Figure 5 shows the computational mesh used for the 22″ rig FEGV configuration for the actuator-duct calculation with a total grid-point number of around 0.3 million. The computational domain is wedge-shaped, with five grid points in the pitchwise direction. Compared with the mesh used in the calculation with the guide vane geometry, the complexity in grid generation was significantly reduced because the geometry detail of the guide vane does not need to be resolved. In addition, the total number of grid points was reduced and therefore the calculation turnaround time was reduced. A periodic boundary was specified on the first and last circumferential planes. Fine grid was packed at the fan duct surfaces to resolve the boundary layer. Within the blade zone, the Navier–Stokes equations were solved with body forces as source terms. Outside the blade zone, the Navier–Stokes equations without the body force terms were solved.

Similar to the preceding CFD calculations, total pressure, total temperature, and swirl profiles were specified at the duct inflow planes. Figure 6 shows the comparisons of total pressure, total temperature, and swirl angle profiles between the actuator duct and CFD predictions. The agreement of total pressure and temperature are very good at the guide vane trailing edge. The predicted swirl angle using the actuator duct is slightly lower than the CFD prediction with the actual guide vane geometry by an average of 2–3 deg. At the fan nozzle exit, there are some discrepancies between predicted *Pt* and *Tt* profiles between the actuator duct and guide vane–geometry results, as shown in Fig. 6. The total pressure and total temperature profiles from the guide vane–geometry calculations show the effect of secondary flow and wake mixing due to the presence of the guide vane. Those flow details cannot be resolved using an actuator duct because the body force coefficients used in the current study are uniform circumferentially.

In addition to the total pressure, total temperature (*Pt*, *Tt*), and swirl profiles, the mass-averaged total pressures and total temperatures were also compared between the actuator duct and guide vane–geometry results. Figures 7 and 8 show the comparisons of the mass-averaged *Pt* at the guide vane trailing edge and fan nozzle

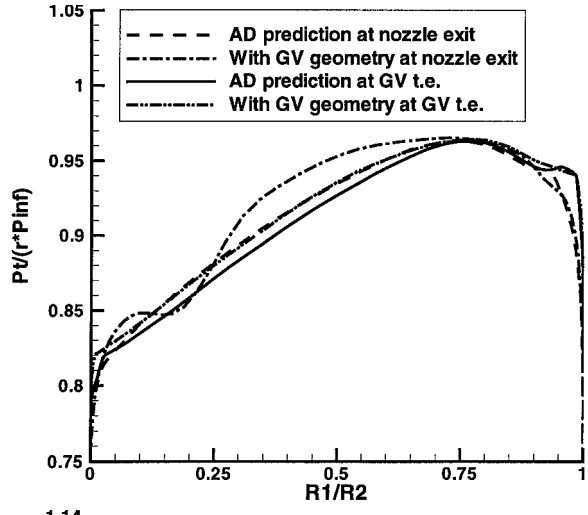

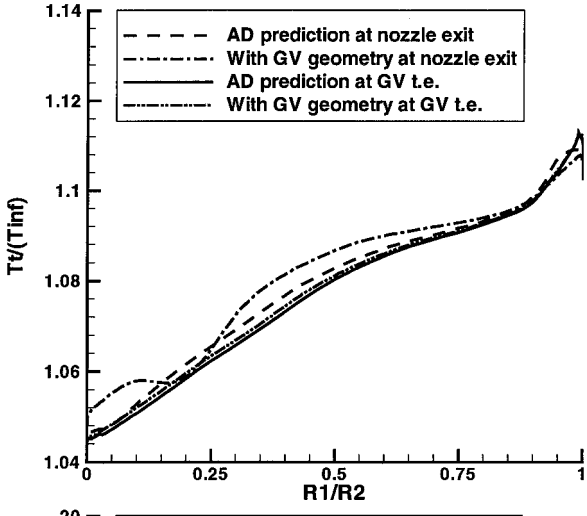

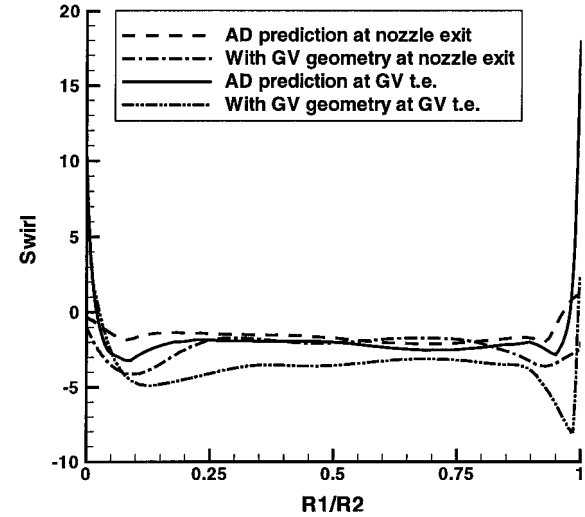

Fig. 6 Comparison of *Pt*, *Tt*, and swirl profiles between actuator-duct and CFD predictions at guide vane trailing edge. Fan-2 at 7870 rpm. $R_1 = r - r_{\text{hub}}$ and $R_2 = r_{\text{casing}} - r_{\text{hub}}$.

exit. Between the inflow plane and the guide vane trailing edge, the actuator duct predicted an average loss 0.2% higher than the guide vane–geometry predictions for the fan-1 configuration. There is no explanation of why the agreement at the guide vane trailing edge is better for the fan-2 configuration than for the fan-1 configuration. Between the guide vane trailing edge and the fan nozzle exit, the actuator-duct model predicted total pressure losses lower than the guide vane–geometry predictions for both configurations because the loss due to secondary flow and wake mixing was not resolved

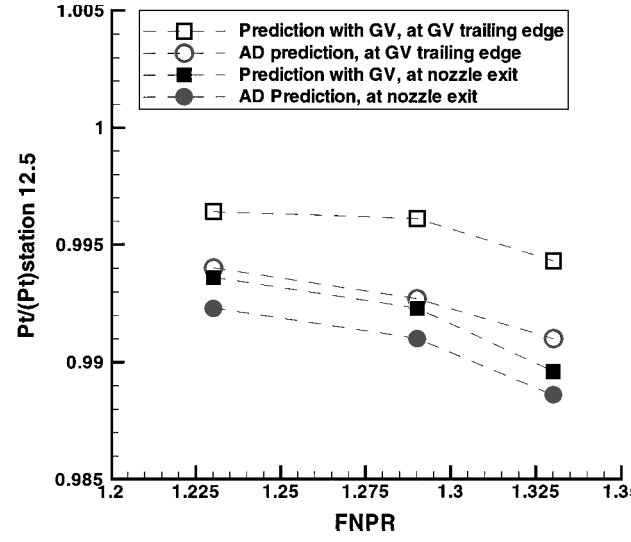

Fig. 7 Comparison of mass-averaged *Pt* for fan-1 configuration.

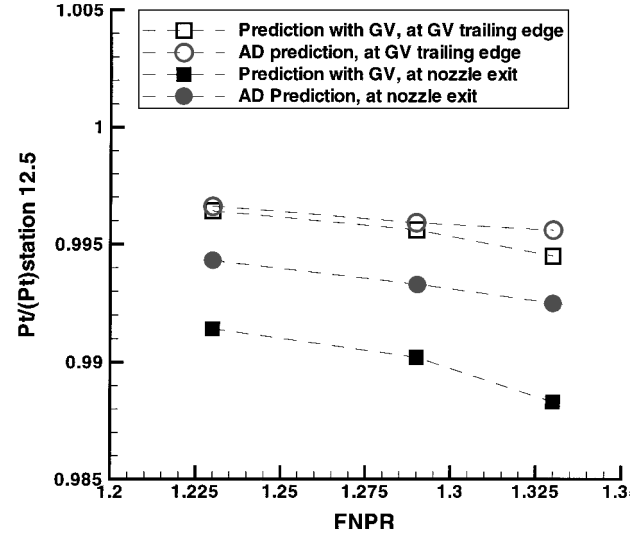

Fig. 8 Comparison of mass-averaged *Pt* for fan-2 configuration.

using the actuator duct. The predicted *Pt* loss between the guide vane trailing edge and nozzle exit is higher for fan-2, probably because the fan-2 configuration has more guide vanes than the fan-1 configuration and therefore the loss due to mixing is higher. For total temperature, both actuator-duct predictions and predictions using the guide vane–geometry show no changes between the inflow plane and the fan duct exit.

The results for the 22″ rig FEGV demonstrated that the body force coefficients generated from the flowfield of the design condition (rpm) can be used for the off-design conditions to predict the flowfields that agree with the CFD predictions. In a future study, body force coefficients generated from the flowfield of the off-design condition (rpm) will be used for the other operating conditions to identify sensitivity of the coefficients to the operating condition. In addition, a more sophisticated mode, such as a nonuniform coefficients profile in the circumferential direction, can be used to include the loss due to secondary flow.

Three-Dimensional NASA 22″ Rig Configuration

In this section, the three-dimensional NASA 22″ rig configuration, as shown in Fig. 9, which includes inlet, fan duct, and fan nozzle, was used for the calculation. The primary objective of the calculation is to validate the actuator-duct logic to simulate the flow through the fan rotor with high inlet distortion. The predicted flowfields were compared with test data for different operating conditions with different fan speeds (rpm) and inlet angles of attack. In

addition, a calculation was performed with a flow-through nacelle configuration based on the NASA 22″ rig. The predictions were compared with those of the three-dimensional 22″ rig to determine the effect of the rotor on the inlet separation angle of attack.

For the NASA 22″ rig, the number of rotor and FEGV blades are 18 and 45, respectively. Flow through the rotor and the FEGV was simulated using an actuator duct without the blade geometry. The total number of grid points of the three-dimensional 22″ rig mesh used for the calculation is around 7 million. The calculations were made for a freestream Mach number of 0.2 with different angle-of-attack and fan speeds. Table 2 shows a matrix of the operating conditions used in this study.

In the calculations, the core duct mass flow rates were specified at the core duct outflow boundary for the 0 deg angle-of-attack cases; the static pressures at the core duct outflow boundary were then calculated from these converged solutions. The resultant static pressures were then used as boundary conditions for the high angle-of-attack calculations, because the mass flow rates measurements were available only for the 0 deg angle-of-attack conditions.

Table 2 Operating conditions for three-dimensional 22″ rig calculations

Fan speed (rpm)	Angle of attack (deg)
8740	0, 28, 32, 34, 35
7740	0, 30, 34, 35, 36
5010	0, 31, 32, 33

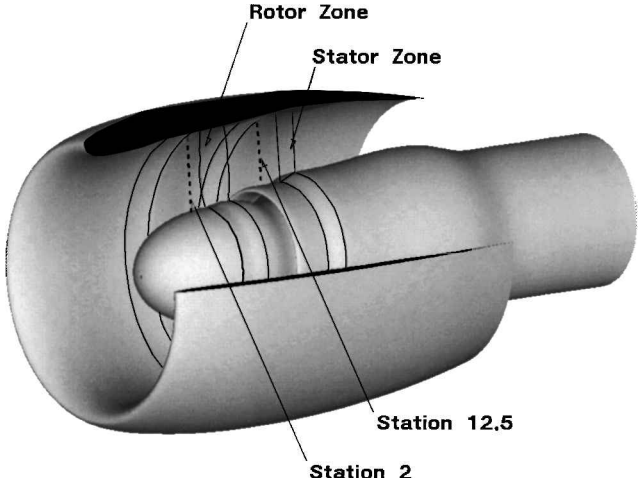

Fig. 9 NASA three-dimensional 22″ rig configuration.

The FEGV body force coefficients were generated from the CFD prediction that used the blade geometry at the 8740 rpm condition, as shown in the preceding section. For the fan rotor, the flowfield around the blade was reconstructed, based on the experimental data at the 8740 rpm condition with 0 deg angle of attack, using the streamline curvature approach. Then the fan rotor coefficients were calculated using Eq. (1) after the body forces were obtained by integrating forces over the computational cell. The rotor and FEGV body force coefficients were then used in the calculations at different rotor rpm and inlet angle of attack.

The actuator-duct logic was assessed by comparing the CFD predictions with test data.[8] The predicted total pressure profiles before and after the rotor (station 2 and station 12.5, as shown in Fig. 9) were compared with the measurements. In addition, comparison of the inlet separation angle of attack was made between the prediction and the test data.

Calculation of 0 deg Angle-of-Attack

Figure 10 shows the predicted total pressure and velocity vector for 8760 rpm at the 0 deg angle of attack. All the flow features of the flow through the fan rotor and stator have been predicted. The total pressure increases as the flow passes through the fan rotor. It also shows that swirl was introduced by the rotor and was reduced by the stator. Figure 11 shows the comparisons of the total pressure, total temperature, and swirl profiles at a location downstream of the fan rotor (station 12.5) for the 8740 rpm condition. In general, the agreements between the predicted and measured profiles are very good. The predicted fan duct mass flow rates were also compared with the test data. The WIND code with the actuator duct predicted fan duct mass flow rates higher than the measurements by 0.5 and 0.7% for the 8740 and 7740 rpm conditions, respectively. For the lowest fan speed (5510 rpm), the predicted fan mass flow is about 1.9% higher than the measurement. This discrepancy is probably due to rotor body force coefficients having been generated based on measurements at a high fan speed (8740 rpm) that may be very different from the flowfield at low rpm (5510 rpm). The difference may also be due to the pressure used at the core duct outflow boundary. The outlet pressure was calculated based on the mass flow rate

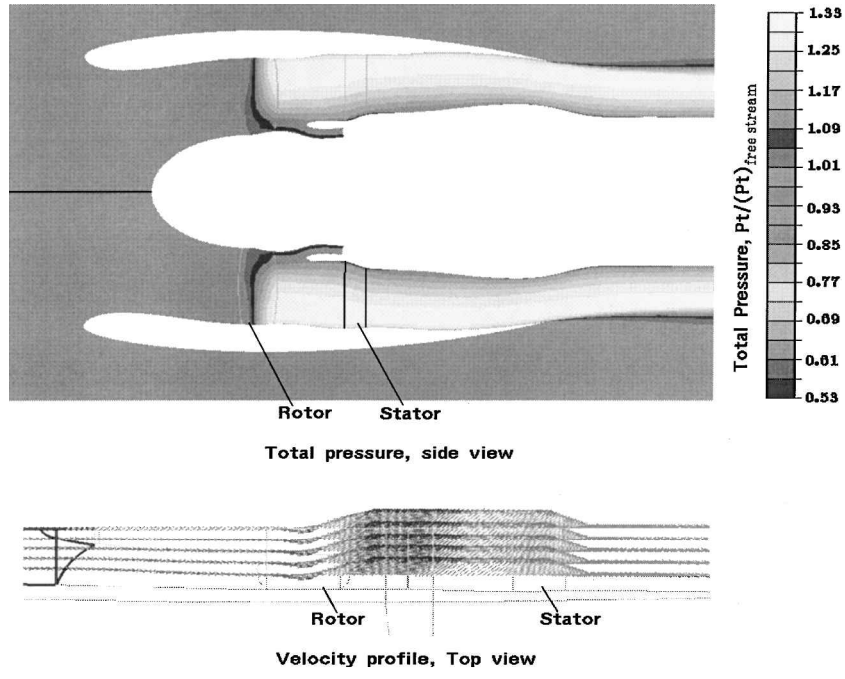

Fig. 10 Predicted total pressure profile and velocity vector for 8740 rpm at 0 deg angle of attack.

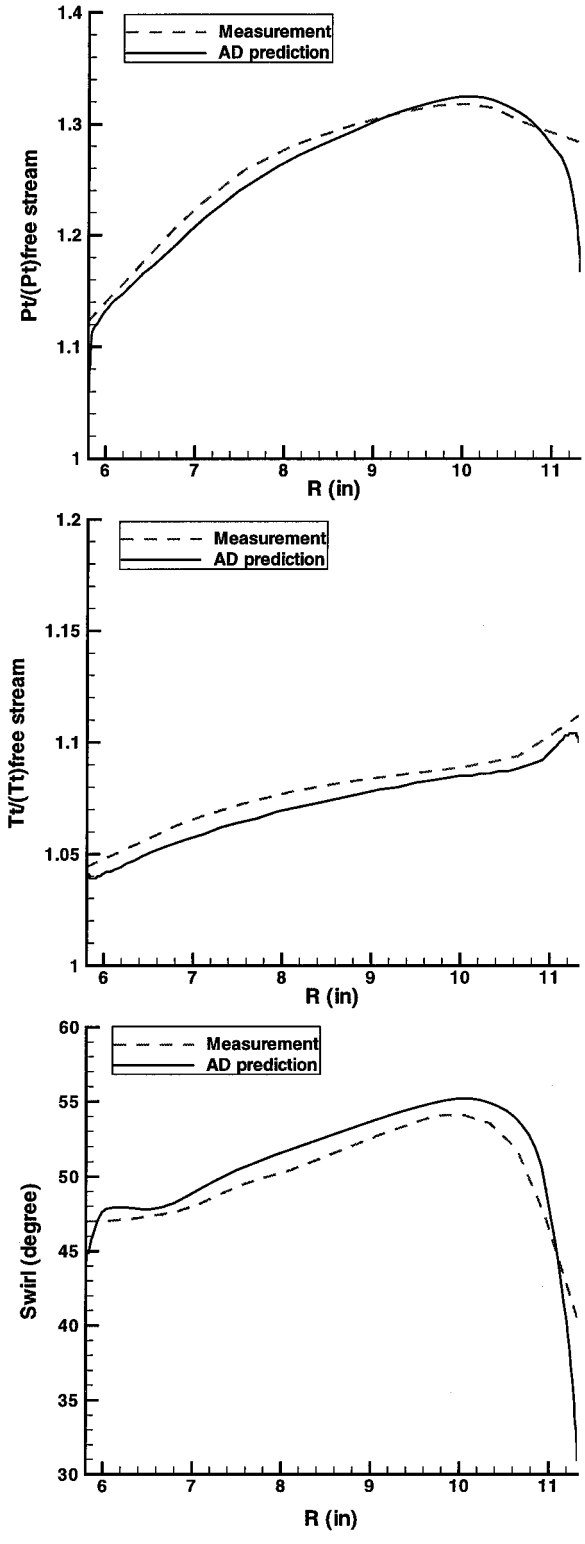

Fig. 11 Comparison of prediction and measurement at station 12.5 for 8740 rpm at 0 deg angle of attack.

at 8740 rpm condition because it is the only measurement available for all conditions. It is noted that all the measured mass flow rates have been corrected for the blockage of the instrumentation rake upstream of the fan, which reduced rig airflow in the experiment by approximately 3%. The current CFD calculations did not include the geometry of the instrumentation rake.

High Angle-of-Attack Calculation

The predicted total pressure profiles upstream and downstream (stations 2 and 12.5) of the fan rotor were compared with the test data for angle of attack. In addition, the predicted inlet separation angles of attack were compared with the measurements. The inlet separation angle was determined by monitoring the wall static pressure along the keel and the total pressure distortion in the diffuser. The total pressure distortion used as one of the flow parameters in the test to determine inlet separation is defined as $((P_t)_{\max} - (P_t)_{\min})/(P_t)_{\inf}$. In the test, $(P_t)_{\max}$ and $(P_t)_{\min}$ were obtained from the total pressure rake located about 4″ upstream of the fan rotor face (station 2). In the analysis, the total pressure distortion was calculated using the predicted total pressure at the computational grid points that were at approximately the same locations as the total pressure probes whose measurements were used to compute distortion. Figure 12 shows the predicted flowfield for the 8740 rpm condition at a 35 deg angle of attack with the boundary layer separated near the hi-light. It is noted that an incipient separation occurred just downstream of the location of peak Mach number at the 34 deg angle of attack. Figure 13 compares predicted and measured wall static pressure distributions. It shows that the test data for the 34 deg angle of attack fall between the predictions of the 34 and 35 deg angles of attack because the prediction indicated attached flow, although a separation occurred in the test for the 34 deg angle of attack. The predicted total pressure

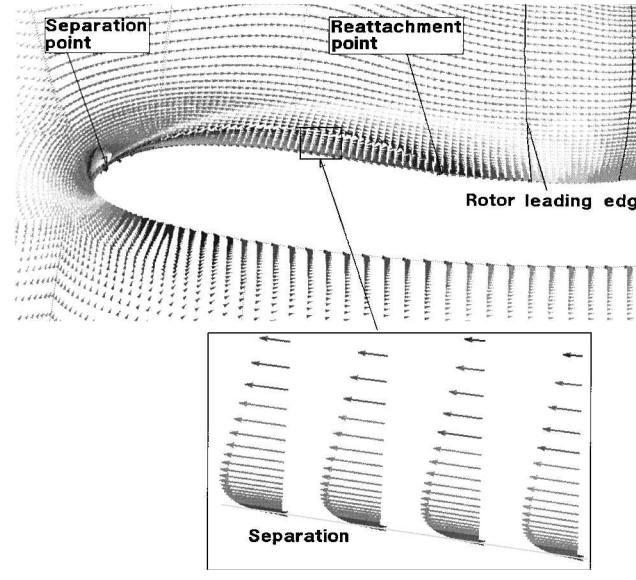

Fig. 12 Predicted velocity profile for 8740 rpm at 35 deg angle of attack.

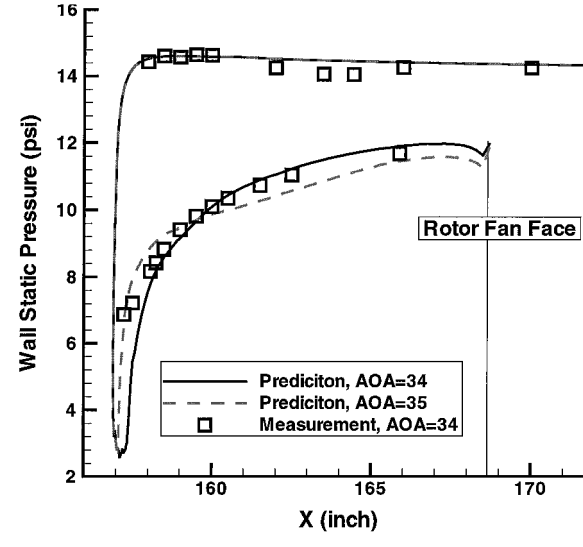

Fig. 13 Predicted and measured wall static pressure distributions at keel, 8740 rpm.

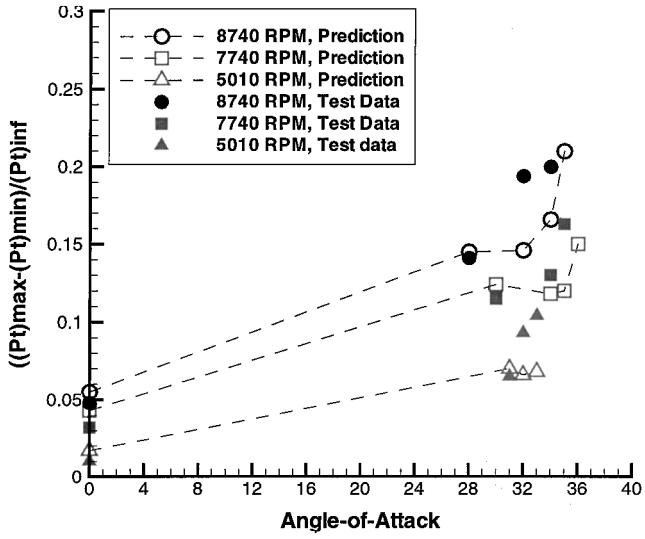

Fig. 14 Total pressure distortion at station 2.

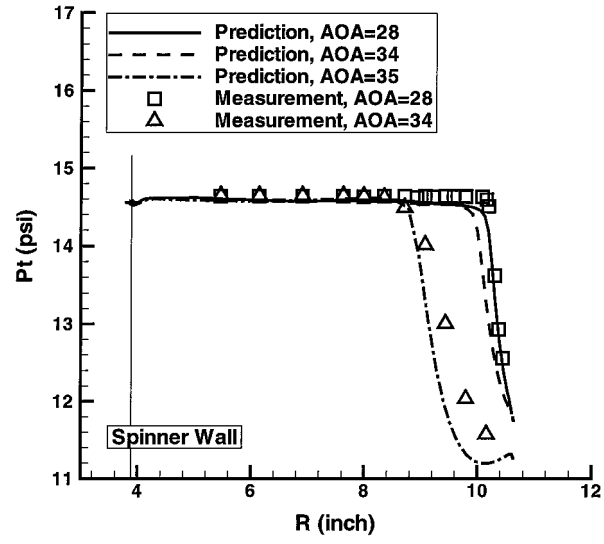

Fig. 15 Comparison of total pressure at station 2, keel location, 8740 rpm.

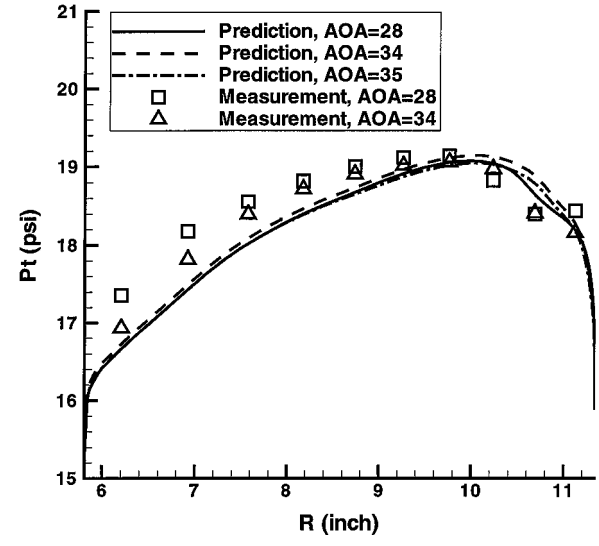

Fig. 16 Comparison of total pressure at station 12.5, θ = 225 deg, 8740 rpm.

distortion shown in Fig. 14 indicates that the inlet flow separated at approximately 34–35 deg at the 8740 rpm condition, and between 35 and 36 deg for the 7740 rpm condition, as shown by the sudden increase of total pressure deficit. For the 5010 rpm condition, no large total pressure deficit in the diffuser occurred before the 33 deg angle of attack. In the calculations for the 8740 and 7740 rpm conditions, the incipient separation occurred about 1–2 deg before significant inlet flow separation. It is very likely that the flow will separate for the 5010 rpm condition at approximately 34–35 deg angle of attack because the incipient separation occurred in the diffuser at 33 deg.

Figure 14 shows that the WIND code with the actuator duct predicted a separation angle-of-attack variation consistent with the measurements for the different fan speeds. The fan speed affects the separation angle of attack in two ways: 1) increasing rotor rpm increases the flow turning speed around the hi-light and therefore decreases the separation-free angle of attack; 2) increasing rotor rpm tends to decrease diffuser separation by a near-wall pumping effect. This may be the reason that the incipient separation occurs in the diffuser for the 5010 rpm condition, but the separation begins near the hi-light for the 8740 rpm condition in the CFD predictions.

It is noted that the predicted separation angles of attack are consistently higher than measurements by about 2–3 deg, which is considered a good agreement because of the high uncertainty in measuring separation angle of attack in the experiment. In the CFD calculations, a turbulent boundary layer was specified on all the nacelle surfaces because no tripping device was used in the test, and the locations of the laminar-turbulent transition were unknown. It is possible that the flow separated in the laminar region in the test, but the CFD predicted attached flow because a turbulent boundary layer was used in that region. The agreement of the separation angle of attack between prediction and measurement may be improved with the use of a reliable transition model in the CFD prediction.

Figure 15 compares the total pressure profiles at station 2 for the 28 deg angle-of-attack case in which both prediction and measurement showed attached flow in the diffuser. Figure 16 shows the total pressure profile at station 12.5 at a circumferential location: $\theta = 225$ deg, which is 45 deg clockwise from the keel ($\theta = 180$ deg). These predictions compare favorably with the measurements at both stations. Similar comparisons for 34 and 35 deg angles of attack are also made in Figs. 15 and 16. Figure 15 demonstrates that the 34 deg angle-of-attack measurement (separated) has better agreement with the calculation at the 35 deg angle of attack (also separated).

Rotor Effect on Separation Angle of Attack

The calculations for a flow-through 22″ rig nacelle were conducted to determine the impact of the fan rotor on inlet separation at high angle-of-attack conditions. The results of the flow-through nacelle were compared with the previous predictions, which used an actuator duct to represent the effect of the fan rotor (powered nacelle). A modified 22″ rig configuration with a constant-area duct attached downstream of the fan duct was used in the flow-through nacelle calculation. The mass flow rate from the previous calculation with rotor effect was used as the outflow boundary condition at the end of the constant-area duct. The calculations were performed for the 8740 rpm condition with angles of attack of 32 and 35 deg.

Figure 17 show the velocity distributions of the flow-through nacelle for 8740 rpm at 35 deg. For the flow-through nacelle, incipient separation occurred at 32 deg, but the boundary layer remained attached for the powered nacelle. As the angle of attack increased to 35 deg, the separation bubble extended to the region downstream of fan rotor for the flow-through nacelle, as shown in Fig. 17, and the separation bubble reattached at the location upstream of fan face for the powered nacelle, as shown in Fig. 12. The comparison of the predicted total pressure distortion shown in Fig. 18 indicates that the presence of the rotor increased the separation-free angle-of-attack over the flow-through nacelle. With the actuator duct, the CFD calculation predicted that the effect of the rotor on separation angle of attack is qualitatively consistent with the observation from the experiment.

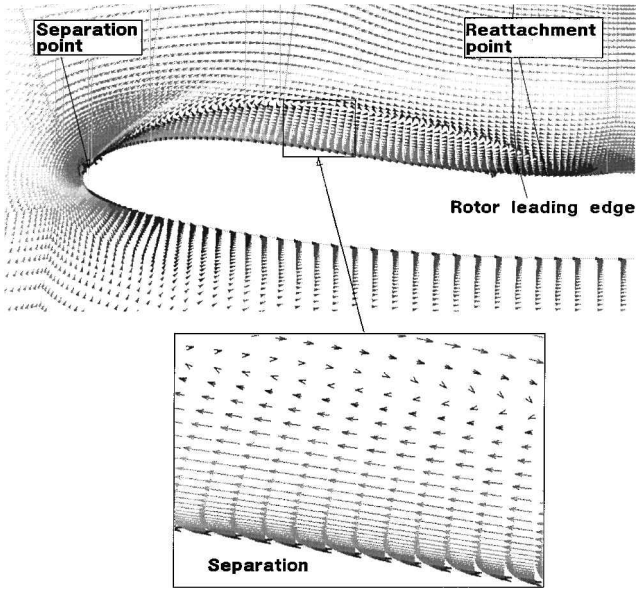

Fig. 17 Predicted velocity profile of flow-through nacelle for 8740 rpm at 35 deg.

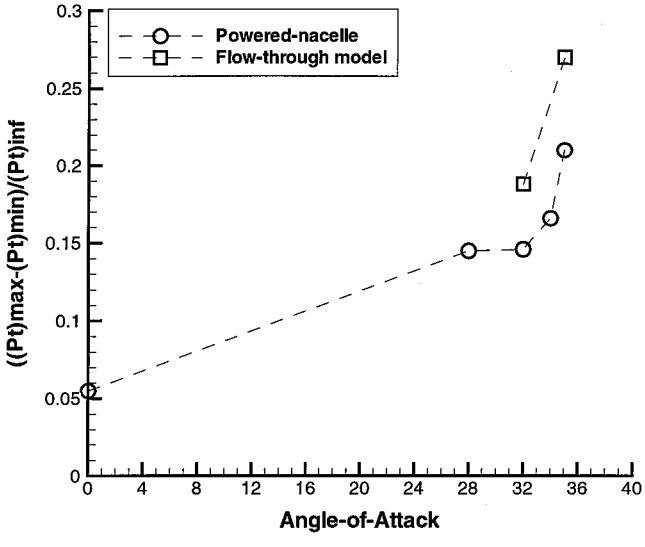

Fig. 18 Total pressure distortion at station 2.

Conclusion

In this study, flow turning and total pressure and temperature changes across the fan rotor and stator were simulated using the actuator duct without the actual blade geometry. This model allows an affordable, accurate prediction of the three-dimensional flowfield through the rotor and stator blades. Assessment and validation of the model, which was carried out with a NASA Stage 35 compressor and a NASA 22″ rig configuration, yields the following conclusions:

1) The actuator-duct model was installed into the Navier–Stokes WIND code correctly.

2) The results indicate that the actuator duct is well suited for certain engineering applications, such as inlet and nozzle flow analysis, of high-bypass propulsion systems. The results of the inlet flow were qualitatively consistent with experiments on the effect of the fan on the angle of attack which separation occurs. This should eventually result in improving subsonic inlet designs.

3) Using the actuator-duct model, grid generation complexity was significantly reduced compared with grid generation requirements when including actual rotor or stator geometry.

4) The numbers of the grid points required are fewer with the actuator-duct model and therefore the calculation turnaround time was reduced.

5) This actuator-duct technology enables a convenient, efficient, and relatively accurate way to include the effect of rotating and stationary axial-flow turbomachinary hardware in propulsion airframe integration.

Acknowledgments

This effort was supported under NASA Contract NAS1-20267. The authors would like to thank M. J. Larkin and G. A. Kohlenberg of Pratt and Whitney for providing test data and T. A. Reyhner and G. C. Paynter of Boeing for their comments on the work.

References

[1]Larkin, M. J., and Schweiger, P. S., "Ultra High Bypass Nacelle Aerodynamics," NAS3-25952, 1992.

[2]Iek, C., Boldman, D. R., and Ibrahim, M., "3-D Viscous Flow CFD Analysis of the Propeller Effect on an Advanced Ducted Propeller Subsonic Inlet," AIAA Paper 93-1847, June 1993.

[3]Bush, R. H., "Engine Face and Screen Loss Model for CFD Application," AIAA Paper, 1997.

[4]Nishizawa, T., and Takata, H., "Numerical Study on Rotating Stall in Finite Pitch Cascade," American Society of Mechanical Engineers, Paper 94-GT-258, 1994.

[5]Hirsch, C., "CFD Methodology and Validation for Turbomachinery Flows," AGARD Rept. AGARD-LS-195, May 1994.

[6]Gong, Y., "A Computational Model for Rotating Stall and Inlet Distortion in Multistage Compressor," Ph.D. Dissertation, Dept. of Aeronautics and Astronautics, Massachusetts Inst. of Technology, Cambridge, MA, 1999.

[7]The WIND Navier–Stokes code, URL: http://www.grc.nasa.gov/WWW/winddocs.

[8]Kohlenburg, G. A., and Larkin, M. J., "Final Report of AST Contract Task 9," *Proceedings of the NASA Contract Report, Task AST-9*, Pratt and Whitney, 2000.

[9]Moore, R. D., and Reid, L., "Performance of Single-Stage Axial Flow Transonic Compressor with Rotor and Stator Aspect Ratios of 1.19 and 1.26 Respectively, and with Design Pressure Ratio of 1.82," NASA TP-1338, 1978.